Int. J. Electrochem. Sci., 10 **(2015)** 10272 - 10291

International Journal of
ELECTROCHEMICAL
SCIENCE
www.electrochemsci.org

Investigating Electrochemical Properties and Interfacial Processes of Manganese Oxides/Graphene Hybrids as High-Performance Supercapacitor Electrodes

S. Gupta[1,*], *M. vanMeveren*[1], *and J. Jasinski*[2]

[1] Department of Physics and Astronomy, Western Kentucky University, 1906 College Heights Blvd. Bowling Green, KY 42101-3576, USA
[2] Department of Chemical Engineering and Conn Center for Renewable Energy, University of Louisville, KY 40292, USA
[*]E-mail: sanju.gupta@wku.edu

Received: 5 August 2015 / *Accepted:* 7 September 2015 / *Published:* 4 November 2015

In this work, we report on the development of novel materials using a combination of known materials with diverse functionality for energy storage applications. We prepared graphene-inorganic 'hybrids' coupled with electrochemically synthesized manganese oxides on graphene oxide and reduced graphene oxide platforms such that each component play a unique and critical function for high-performance. A range of complementary characterization tools reveal the surface morphology, local (lattice dynamical) and average structure, and local charge transfer due to adsorbed manganese oxides highlighting the surface structure and interfaces of hybrids. The electrochemical performance of the graphene-based hybrids as asymmetric supercapacitors is evaluated by cyclic voltammetry and impedance techniques exhibiting nearly rectangular cyclic voltammograms superimposed with redox peaks from manganese oxides with an average specific capacitance of > 550 Fg^{-1} and it was charged / discharged within seconds or < 1 minute. We also determined the electric-double layer or interfacial capacitance, charge transfer resistance and low frequency capacitance. The results demonstrate that this facile approach affords chemical adsorption thus expected to have synergistic coupling between the pseudocapacitive / supercapacitive components and displaying stable high-performance behavior attributed to reasonable density of tailored interfaces. Scanning electrochemical microscopy allowed mapping enhanced electrochemical activity/(re)activity of surface ion adsorption at solid/liquid interface.

Keywords: Electrochemical deposition, Manganese dioxide, Supercapacitor/ Pseudocapacitor, SECM, Graphene derivatives.

1. INTRODUCTION

An intense research activity on alternative energy sources is stimulated by continuously increasing global demand on electrical energy. The electrochemical energy-storage devices (EESDs) including supercapacitors and batteries represent some of the most efficient and environmentally benignity technologies [1, 2]. Supercapacitors play a vital role as efficient energy storage and conversion devices due to their coexisting larger power and energy density which fills the gap between traditional capacitors and batteries. As a result, the development of advanced electrodes of novel functional materials with higher performance becomes indispensable. The breakthroughs happen when advanced materials or combinations of known materials with multi-dimensionality and functionality are created.

Graphene, a single atomic layer of sp^2-bonded carbon (sp^2 C) hybridization where carbon atoms are bonded together forming a hexagonal lattice that resembles a honeycomb, has received considerable attention owing to superlative physical-chemical-electrochemical properties towards diverse applications [3,4,5]. It exhibits remarkable mechanical strength and flexibility (Young's modulus ~ 1TPa) [6] and high theoretical specific surface area (2,630 m^2 g^{-1}) [7] suitable for super (ultra)capacitors [8] and Li-ion batteries electrodes [9]. In addition to traditional monolayer graphene, it can be modified through a variety of physical and chemical interactions enabling various graphene-derivatives and graphene related materials with tailored and desirable properties [10]. Graphene oxide (GO) [11] and reduced graphene oxide (rGO) [12] are some of the emergent variants as functional nanoscaffolds in energy-related research namely, hydrogen-based energy storage devices [13], supercapacitors [14,15] batteries [16], solar cells [17], and fuel cells [18,19] besides chemical and biological applications [20,21, 22]. In fact, GO is potential candidate for large-area electronics and nancomposites due to easy solution processability and therefore can be readily and uniformly deposited on a range of substrates and further reduced by various means. While GO is considered electrically insulating due to the presence of saturated sp^3-bonded carbons (sp^3 C) bonded to oxygen moiety and a disordered analogue of the highly conducting crystalline graphene with oxygenated functional groups (carboxyls or –COOH and epoxides or -ROOH at the edges and hydroxyls or –OH on the surface), its reduced form (rGO) contains residual oxygen (~ 8 *at.*%) and possibly amine groups from hydrazine monohydrate offer tunable electrical conductivity over several order of magnitude. Nevertheless, the covalently bonded oxygen functional groups give rise to remarkable mechanical strength [23, 24] along with molecular-level chemical-biological sensing capabilities [25,26,27]. The C-O bonds possess varying chemical activity/reactivity over the graphene layer surfaces based upon the local hybridization that owes to electron-withdrawing the effect of sp-hybridized oxygen (*i.e.* carbonyl group) and donating effect of sp^2-hybridized oxygen (*i.e.* alcohol group). In addition, the presence of remaining sp^3 C sites in rGO hinders the flow of charge carriers through sp^2 C clusters so that the electrical transport occurs primarily by hopping rather than near ballistically [28] as is the case for mechanically exfoliated traditional monolayer graphene. However, these chemical modifications tailor the surface–chemistry to specific applications including hdyrodrophilic *versus* hydrophobic (GO) that facilitates feasible interactions and surface and interface structure dependent electrocatalytic activity especially, when combined with other nanoscale materials [27, 29, 30]. To mention, while the

exact electronic structure of GO and rGO is limited due to lack of detailed knowledge on bonding configuration, random location of the residual oxygen, number density and type of defects generated during oxygen evolution, nature of hybridization states of C-C and C=O bonds and spatial distribution, it does not prevent their development with other materials forming hybrids with facile surface structure and creating tailored interfaces for electrochemical energy storage applications presented in this work. It owes to the proliferation of portable consumer electronics, where much effort has been devoted to lightweight, flexible and wearable electronics (*i.e.* wearable displays, artificial electronic skin, and distributed sensors) to meet the growing demands of modern digital society on the electrical energy storage systems [31, 32].

While typical supercapacitors electrodes are based on a gamut of nanocarbons (*e.g.* activated carbon, porous carbon, carbon nanotubes, graphene and related materials) as active material [33,34,35,36,37,38] occasionally they are limited by themselves as high-performance systems in terms of energy density. Likewise, pseudocapacitive (alternatively, redox- or electroactive) materials include metal oxides, metal hydrides, metal hydroxides and conducting polymers are explored that are limited in power density. It is noteworthy that in practical supercapacitor electrodes, the two energy storage mechanisms often work rather concomitantly. To address these issues, graphene-based hybrid composites are considered in an effort to overcome the charge-storage limitations and poor cycling behavior, where loading of electroactive materials allow substantial higher storage capacities than those of bare graphene. For the hybrid composites, graphene act as support for the growth of redox-active nanostructures facilitating uniform deposition and optimum loading that in turn hinder re-stacking (or agglomeration) by lowering the van der Waals forces among the graphene layers and helps in shuttling electrons involved in redox reactions during electrochemical processes thus enhancing the performance in terms of specific charge storage capacity and charge-discharge cyclability. Metal oxides (MeO_x) are attractive since they offer higher specific capacitance, wide operational potential window (required for Faradaic redox reactions) and stability through multiple charging-discharging cycling. Among several redox-active materials (Me = Ru, Ti, Mn, Co, V, Fe, Ni, Mo etc.) [39,40] recent research has evidenced that manganese oxide polymorphs (*i.e.* MnO_2 and Mn_3O_4) appear to promising with advantages of cost effective, scalable synthesis and simple processing, environmental benignity (harmful only by excessive inhalation), rich electrochemical properties such as rapid charging-discharging with various oxidation states ($Mn^{2+}/Mn^{3+}/Mn^{4+}$) [41]. Mn_3O_4 is a mixed-valence oxide which adopts a tetragonally distorted spinel structure at room temperature and pressure [42]. The other polymorph MnO_2 possesses rutile crystal structure with three-coordinate oxide and octahedral metal centers [43]. Graphene-based hybrid materials expand the scope of graphene applications as synergistic effects can result from the interactions (covalent, electrostatic or weaker physisorption and proximity) [44, 45] between graphene and MeO_x supported onto graphene creating tailored interfaces [46, 47, 48, 49, 50].

Most graphene-based hybrid composites are prepared following chemical routes and despite substantial research activity, the insights into establishing structure and properties relationship keeping in view of surface and local charge transfer and interfacial aspects is limited. Moreover, recently metal adatoms and metal clusters on graphene surface have been a topic of great interest since they are expected to locally dope or modify the band structure. In this work, we employed facile approach of

electrochemical deposition of manganese oxide nanostructures on graphene derivatives as support to form hybrid supercapacitors affording stronger chemical attachment. They are expected to have coupling between the pseudocapacitive transition metal oxides and supercapacitive graphenes with additional electrolyte transport paths for electron transfer and proton / cation diffusion showing enhanced electrochemical performance due to the interconnected tunnel crystal phase and reasonable areal density of tailored interfaces. These hybrid supercapacitors are investigated in terms of electrochemical and electrochemical microscopy properties to establish *microscopic structure-property-function* correlations highlighting the surface structure and interfacial process.

2. EXPERIMENTAL

2.1 Materials and Methods

2.1.1 Synthesis

We prepared architectures using electrochemical approach depicted in Fig. 1 and the fabrications details are described as follows. To fabricate thin films of GO, rGO and hybrids, GO was synthesized from natural graphite by the modified Hummers method followed by chemical reduction using hydrazine monohydrate giving rise to rGO [51, 52, 53]. We made suspensions / dispersions of 10 mL each of typical concentration of 0.085 mg/mL in Milli-pure (Milli-Q) water and sonicated for 1 hr at room temperature. After the preparation of colloidal suspensions of individual GO and rGO nanoplatelets, the GO and rGO was deposited by spray-coating for 5 and 10 coats on carbon fiber cloth and ITO coated class substrates of thickness 1 mm and surface area of 1 cm^2 (2 cm x 0.5 cm). After the deposition of GO and rGO, a thin film of MnO_x (possibly MnO_2) was deposited using potentiodynamic cyclic voltammetry; CV between potential window of–1.6 V and 0 V in 0.05 M $(CH_3COO)_2$ $Mn.4H_2O$ solution dissolved in 0.1 M Na_2SO_4 aqueous electrolyte in a typical three-electrode electrochemical cell with Ag/AgCl as a reference electrode (KCl saturated), Pt-wire as a counter electrode and the pre-prepared GO (and rGO)/C fiber cloth (and ITO) as a working electrode. The mass loading of MnO_2 is controlled by adjusting the total charge passed through the electrode and number of cycles during deposition process and selected to 100 μg cm^{-2}. All CV growth experiments were performed at a scan rate of 50 mV/s using a potenitostat/galvanostat electrochemical workstation (CH Instruments Inc. Model 920D) [see Fig. 1].

2.2 Characterization

The surface morphology of the samples studied was characterized using a scanning electron microscopy (SEM) taken on JEOL (Model JEOL 5400LV, MA) instrument operating with thermionic emission gun (Tungsten filament) at primary electron acceleration voltage (V_{acc}) of 15 kV with constant current of 45 μA in secondary electron imaging (SEI) mode collected with an in-lens detector that is equipped with an X-ray ISIS EDS (X-ray energy dispersive spectroscopy) system. The crystallinity of the deposited films was determined by means of X-ray diffraction (XRD) using (Siemens, Model D2000) diffractometer in θ–2θ geometry with Cu K_α radiation (λ = 1.5405 Å)

ranging 5°–70°. Samples were run at a scan rate of 0.04°/second and 0.02°/second, if initial measurement contained unacceptably noisy data. Samples for transmission electron microscopy (TEM) and selected-area electron diffraction (SAED) were prepared by placing one or two drops from as-deposited samples on commercial lacey carbon Cu grids (Ted Pella Inc. CA) and allowing it to air dry.

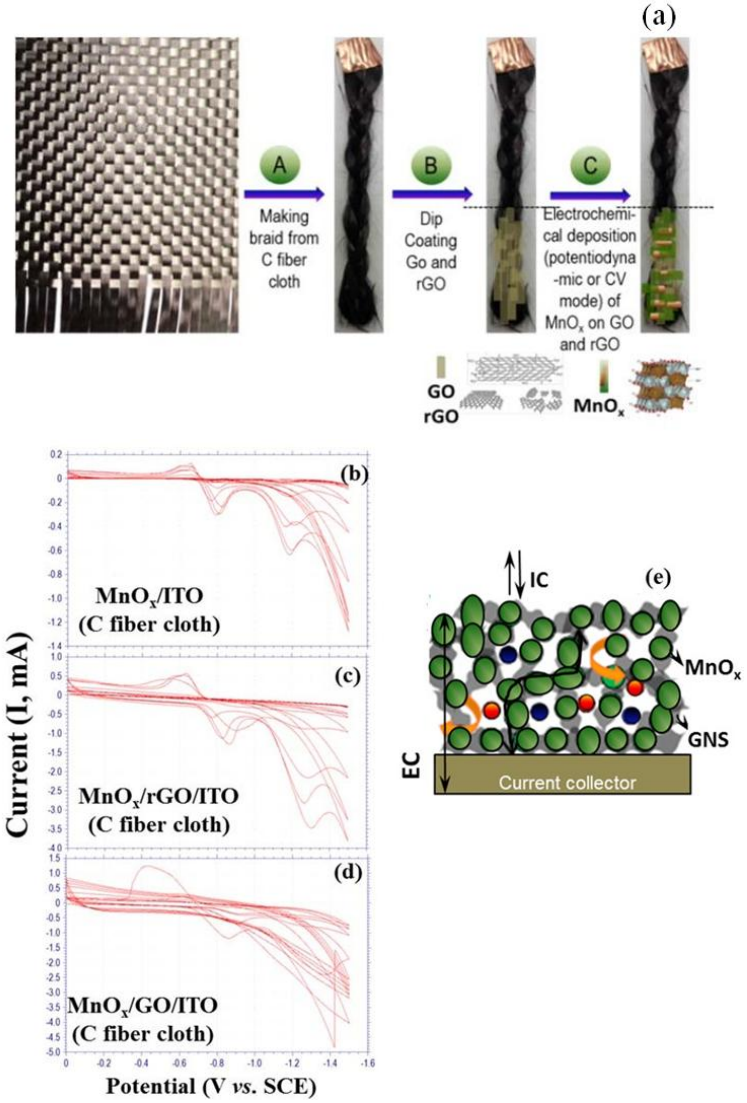

Figure 1. Schematic of (a) electrochemically synthesized manganese oxide nanostructures on braided carbon fiber cloth and cyclic voltammograms 10 cycles between 0 and −1.6V at scan rate of 50 mV/s in 0.5 M Na_2SO_4 aqueous electrolyte and 0.05 M $Mn(OAc)_2$ precursor (b) by itself, MnO_x in 10 cycles (c) on 10 coats of rGO and (d) on 10 coats of GO, all deposited on carbon fiber cloth and/or ITO coated glass substrates. (e) A cartoon of rational design of high-energy high-power hybrid supercapacitor electrodes improving the ionic current (IC) and electronic current (EC) within the electrode *via* growing MnO_x nanostructured and interconnected graphene nanosheets (GNS) including GO and rGO network with high surface area and higher electronic conductivity.

TEM measurements provided nanoscaled structure morphology and help to determine interplanar spacing semi-quantitatively. TEM images and selected area electron diffraction (SAED)

patterns were acquired using a JEOL 1400Plusinstrument. For SAED, we used 0.20 μm aperture with a small spot size and spread beam to increase the electron coherence length at the sample. The SAED ring pattern was transformed in intensity versus interplanar spacing profile using Digital Micrograph (v.3.0) software. The Raman spectra were recorded using a micro-Raman spectrometer (Model InVia Renishaw *plc*, UK) equipped with excitation laser of wavelength 632.8 nm (or energy E_L = 1.92 eV) and power of maximum 18 mW (~4–6 mW incident at the sample), with edge filters cutting at ~100 cm^{-1}. The scattered light from the sample is collected in backscattering geometry, transmitted by a beam splitter and detected by CCD camera. An objective lens of 50x was used providing spot size of 2–3 μm. Extreme care was taken to avoid sample damage or laser induced thermal degradation. The reflected light is filtered using an edge filter to remove the laser excitation and sent to a spectrometer. Raman shift was ranged from 200 cm^{-1} to 3200 cm^{-1} for Co containing hybrids and for GO and rGO it was kept between 1150-3200 cm^{-1} with spectral resolution of 1 cm^{-1}. The acquisition time per pixel was a few minutes to slightly less than an hour. The data was analyzed using Jandel Scientific Peakfit software and WiRE4 software in-built fitting, both based on Marquardt-Levenberg method. Raman spectra determined the lattice vibration characteristics at various areas of interest on the nanostructure and hybrid coating surfaces. Allowing more detail and a greater understanding of the interaction between graphene-related materials and manganese oxides, we also measured room temperature electrical properties (*i.e.* I–V). We made electrical contacts with colloidal silver paste and attached a Cu wire for connection with Keithley 2400 source meter (Keithley, OH). We measure two point contact resistance and determined room temperature electrical conductivity (σ_{dc}) of all of the samples studied. The electrical conductivity for these hybrid films has been measured ranging 0.05-1 S/cm. The surface composition of the samples (at. %) was also determined by XPS (x-ray photoelectron spectroscopy) and the data was acquired using a VG Micro Tech ESCA 2000 X-ray photoelectron spectrometer and EDS. For the XPS measurements, the dispersion solutions were deposited onto silicon substrates to form hybrid thin films, respectively (not shown). A asymmetric three-electrode cell configuration was employed for electrochemical measurements in potentiodynamic cyclic voltammetry (CV), galvanostatic charging-discharging cycling, amperometric and *ac* impedance spectroscopy (*ac* EIS) modes, where a saturated Ag/AgCl (3M KCl) electrode and Pt wire of 3 mm diameter were used as the reference and counter electrode, respectively. Hybrid films of MnO_2/GO (and rGO) on ITO coated glass slides and carbon fiber cloth were used as the working electrodes. Cyclic voltammetry (CV) was performed in 1M Na_2SO_4 aqueous electrolyte within the potential range of –0.8 V and +1.0 V as a function of scan rate, v = 5, 10, 20, 50, 80, 100 and 500 mV/s. Galvanostatic charge-discharge cycling was conducted at constant current densities of 1–10 mA cm^{-2} between 0–1 V. The applied ac amplitude for EIS measurements was 10 mV root mean square in a frequency range of 0.01 Hz to 100 kHz at +0.2 and +0.4 V. Cyclic voltammetry gravimetric specific capacitance (C_s) was calculated from dividing the capacitive charge (Q), obtained using half the integrated area of the CV curve, by the film mass (m) and the width of the operating potential window (V) using equation (1): C_s Q / m.ΔV $F.g^{-1}$. Chronopotentiometry discharge specific capacitance Cs values were calculated by using charge-discharge current (I), potential change with discharge time (dV/dt) and the mass of the deposited film according to the equation (2): C_s = I dt / m.ΔV $F.g^{-1}$. The SECM measurements are carried out (CH Instruments Inc., Model 920D) in feedback and probe approaching modes. For SECM,

we used a Pt microelectrode (~5–8 μm) as the probe working electrode (tip) and a redox mediator, 10 mM $K_3Fe(CN)_6$ (potassium ferricyanide; $Fe(CN)_6^{3-}$) in support electrolyte 1M KCl, for detecting kinetic differences. $K_3Fe(CN)_6$ has a standard potential E^0 = 0.21 V versus Ag/AgCl, thus the Pt tip electrode will be held at a potential of E_t = –0.2 V *versus* Ag/AgCl to ensure complete diffusion-limited oxidation of the Fe(II), species originally present in solution, to Fe(III). The supercapacitor electrodes were biased at V_S = +0.5 V versus Ag/AgCl to ensure complete reduction of the species generated at the micro-tip. The tip was scanned over the working electrode surface area 600 μm x 600 μm at a constant tip-substrate separation of ≤ 40 μm to generate a feedback image with an approximate resolution of the radius of the tip (~ 5 μm).

3. RESULTS AND DISCUSSION

3.1 Structure and Morphology

Figure 2a shows SEM images of MnO_x, GO, rGO, and MnO_2/GO (rGO) films on C fiber cloth including bare substrate. While the electrodeposited MnO_2 film shows surface with spherical aggregates and flower-like (/radiated spherulite) morphology, the GO and rGO film show overlapped nanoplatelets with crumpled morphology. Meanwhile, the potentiodynamically deposited MnO_2 particles show aggregates along with graphene nanoplatelets, preferably on the energetically favorable sites such as defects, functional oxygen moieties and edges. Figure 2b shows TEM images of MnO_2/GO (and rGO) films with thin film of MnO_2 as nano-aggregates adhered to the sheets of GO and rGO nanoplatelets. In the images of Figs. 2a and 2b the presence of MnO_2 polymorph is apparent, while it tends to diminish in size and be less densely packed with the deposition on the GO and rGO nanosheets. This means that the presence of underlying graphene layers leads to more efficient utilization and deposition of finer structure of nanocrystalline MnO_2. It is noteworthy that the relatively lesser closely packed and finer nanostructured phase of electrodeposited MnO_2 is generally necessary favorable as they are mechanically robust and conductive electrodes with large specific surface area for supercapacitor applications facilitating easy penetration of ions through the bulk of the active electrode material. Moreover, these images show well-dispersed nanoparticulates anchored on the graphene sheets/flakes/nanowalls. Figs. 2b and 2c shows SAED patterns and the variation of ring intensity versus interplanar spacing displaying diffuse ring and various peaks associated with both graphene-based systems and MnO_2. Most of the peaks of hybrids show graphene and graphene oxide peaks at 1.06 Å, 1.23 Å, 1.66 Å, 2.12 Å, 3.12 Å, 3.50 Å and 4.41 Å [48]. From the TEM nanoscale surface morphology, it is apparent that the metal oxide nanoparticles are laid upon the nanosheets/nanowalls/nanoedge/ nanofolds of GO and rGO. The SAED pattern reveals quasi-single crystalline nature of Mn oxides with rock salt and spinel structure that are indexed suitably in agreement with the XRD discussed below. On the other hand, the well-resolved lattice fringes / rings in SAED give an interplanar spacing of 0.57 nm, 0.51 nm, 0.35 nm, 0.24 nm and 0.213 nm in good agreement with the distance of (111) (200) and (220) planes for MnO_2. Overall, in most of these patterns there is a dominant crystal phase with random orientation, which seems to have fcc-type rings (space group, *Fm*3*m*) [54, 55].

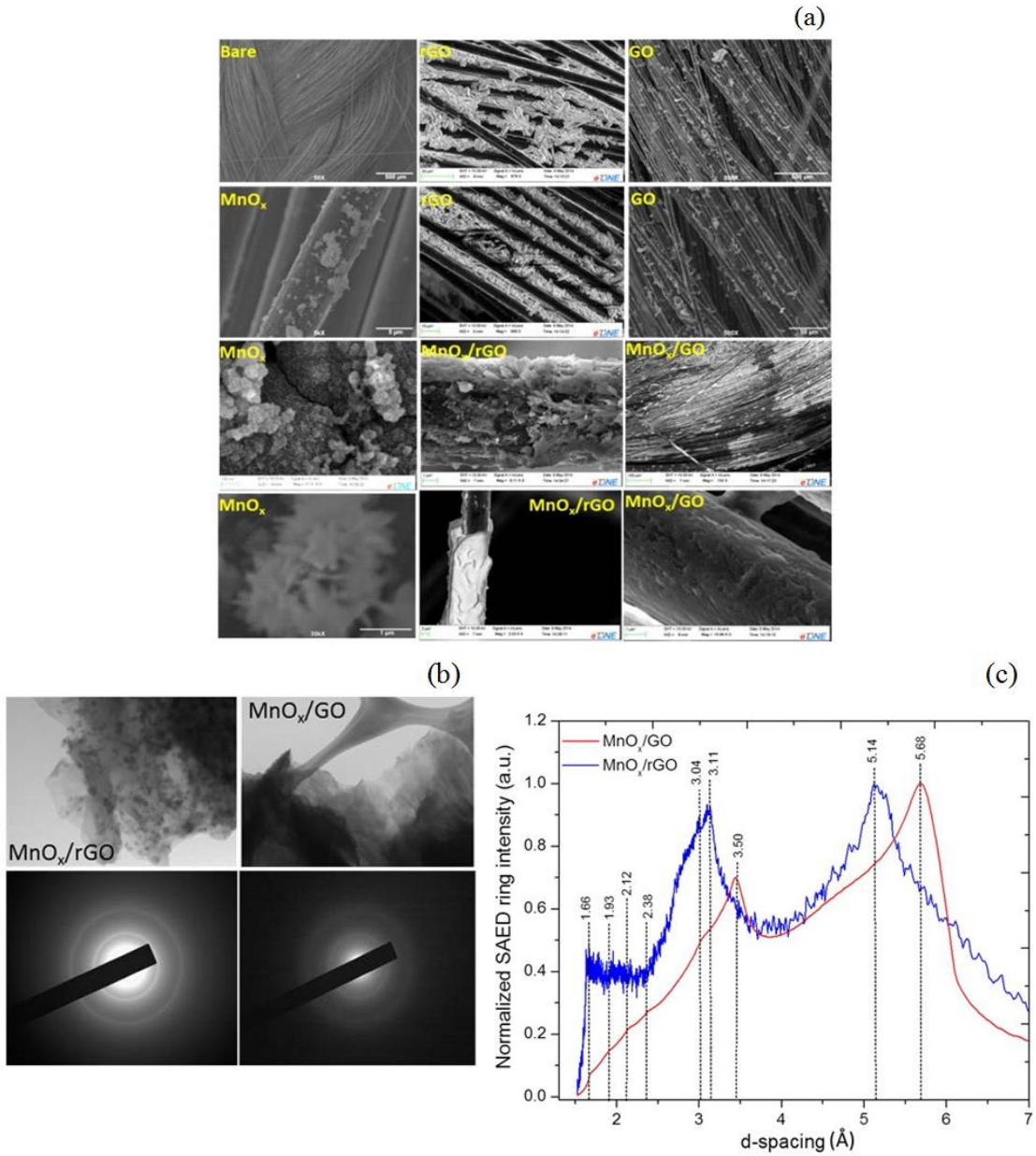

Figure 2. SEM images of (a) bare carbon fiber cloth, GO, rGO, electrochemically synthesized MnO_x, MnO_x/rGO and MnO_x/GO hybrids revealing fiber strands, flower-like morphology of MnO_x, graphene nanosheets and nanowalls coated with MnO_x. (b) TEM images taken with 100 kV along with SAED patterns with an aperture size of 200 nm for representative samples of MnO_x/rGO and MnO_x/GO exhibiting surface morphology at nanoscale exhibiting surface modulations and corrugations. (c) The corresponding diffraction ring intensity pattern versus interplanar spacing (d_{hkil}) is also provided. Scale bars for TEM and SAED images are 10 and 5 nm, respectively.

Figure 3 displays the x-ray diffractograms of MnO_2 and MnO_2/GO (and MnO_2/rGO) films deposited on C fiber cloth substrate. Compared to peak emerge from C fiber substrate at around 16.6^o and 25^o, no obvious diffraction peaks can be observed in the patterns of MnO_2/GO (and rGO) and/or MnO_2 films. The former peak corresponds to an interlayer distance of 0.74 nm for GO that is larger spacing than that of parent graphite or graphene layer (0.34 nm) attributed to the lattice expansion consistent with oxidation of the graphene sheets and possible intercalation of water molecules held in

the interlayer galleries of hydrophilic GO sheets. On the other hand, rGO contains very broad reflection peak at $2\theta = 24.5^{o}$ correspond to d = 0.36 nm, indicating restacking of graphene platelets or sheets to form a multilayer graphene. Besides the deposited particles of MnO_2 are of sufficient larger grain size to have crystalline structure with various diffraction peaks indexed to (002), (311) and (440) reflections characteristic of pyrolusite MnO_2 crystal structure. The crystallite size is obtained from XRD analysis using Debye-Scherrer equation following the relation: $L_{hkl} = K\lambda/\beta_{hkl} \cos\theta_{hkl}$, where L_{hkl} is the crystallite size in nm, λ is the wavelength of Cu K_α, β_{hkl} is the full-width at half-maximum and K is the shape constant and it is equal to 0.94.

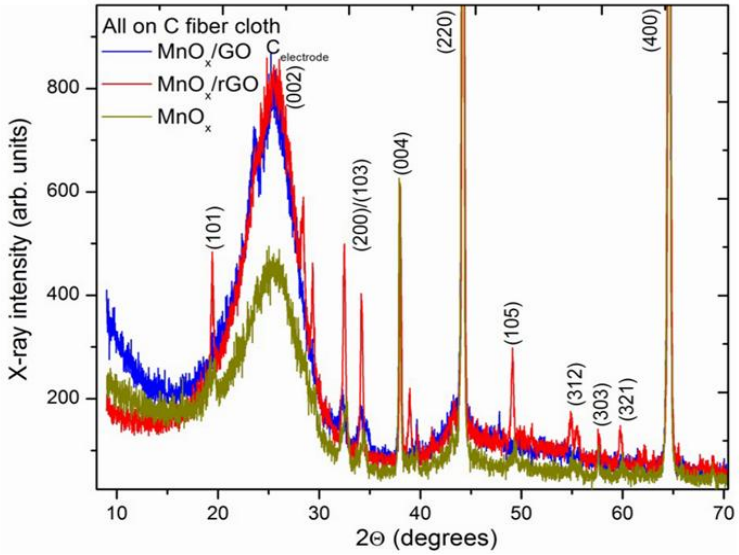

Figure 3. XRD diffractograms for electrochemically synthesized MnO_x, MnO_x/rGO and MnO_x/GO (front and back side of samples) hybrids showing characteristic peaks. The peaks are marked with rectangular box and their (hkl) index. All of the diffractograms are taken in θ-2θ geometry with Cu K_α X-ray source (λ = 1.5405 Å).

The diffraction peaks of hybrids are broad and of low intensity while preserving phases of the constituents implication of forming truly composites. The peak at $2\theta = 36.14^{o}$ is used to determine the lattice spacing (d_{hkl}) and particle size of hybrids which are averaged 90 and 110 nm for GO- and rGO-based hybrids, respectively.

Raman spectroscopy (RS) is a sensitive technique to monitor crystallization and it is used to gain information about the structure of precursor phases, local structural disorder and defects in the graphene sheets and of the hybrid composites. Figure 4 represents Raman spectra of graphene and its derivatives, MnO_2/GO and MnO_2/rGO hybrids besides bare substrate. In general, the spectrum of GO and rGO consist of four primary bands typical characteristic of sp^2 C material, a D-band at 1352 cm^{-1} and two overlapped bands appear at about 1585 and 1611 cm^{-1} assigned for G and D′ bands, respectively, second-order 2D band at 2640 cm^{-1} and combination (D+G) band at 2920 cm^{-1}. The D band is attributed to the defects due to the finite crystallite size or edges of graphene layers, while the the G band is due to in-plane bond-stretching motion of sp^2 C atoms indicative of the presence of ordered graphene layers [56, 57].

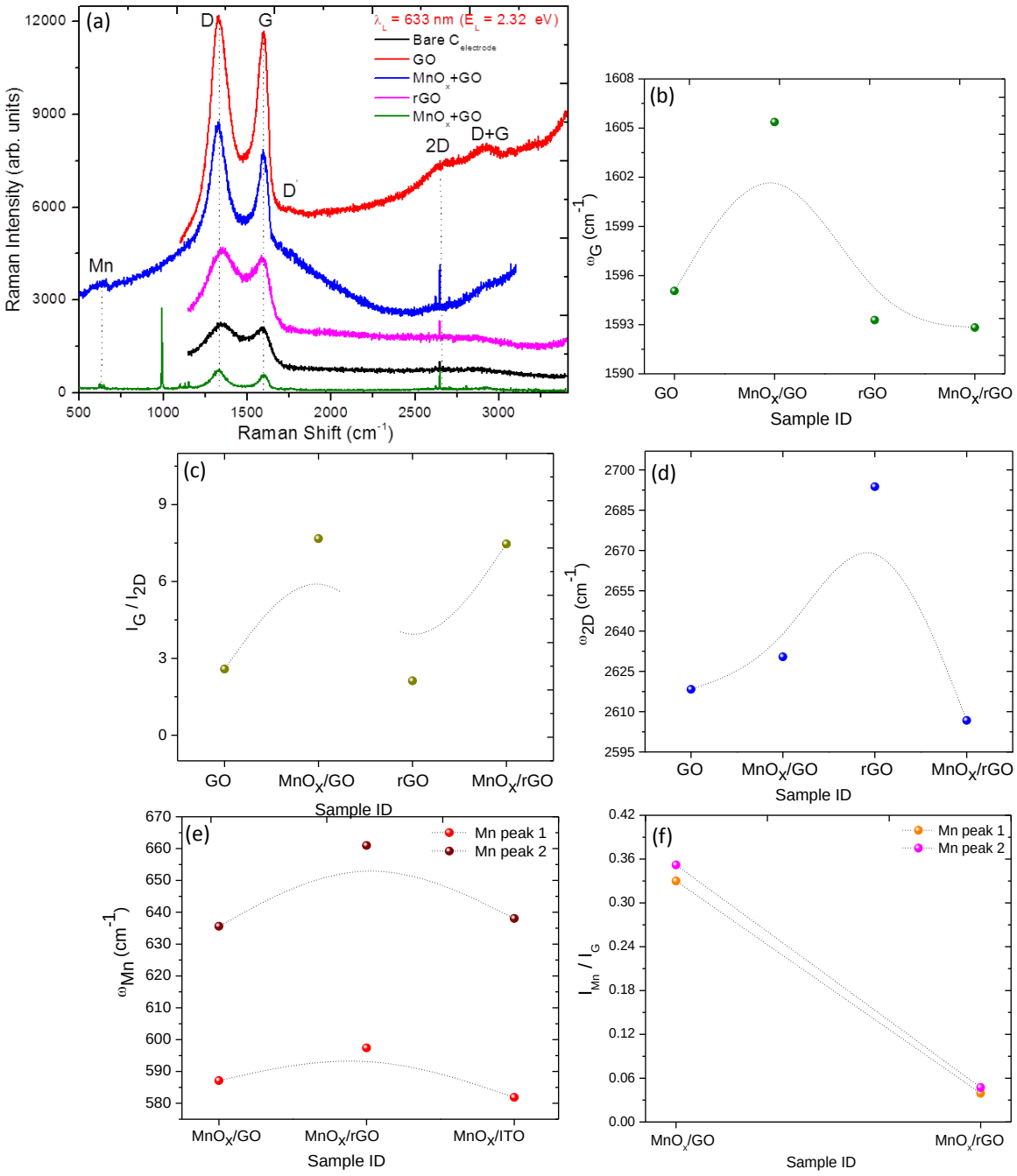

Figure 4. (a) Representative micro-Raman spectra excited at 633 nm wavelength (E_L =1.92 eV) showing characteristic peaks for bare carbon fiber cloth, GO, rGO, electrochemically synthesized MnO_x, MnO_x/rGO and MnO_x/GO hybrids within 300–3200 cm^{-1} spectral window showing characteristic peaks associated with Mn, D, G and 2D, and D+G bands. Raman spectral analysis in terms of (b) G band position (ω_G), (c) intensity ratio of G to 2D band (I_G/I_{2D}), (d) 2D band position (ω_{2D}), (e) bands associated with Mn (ω_{Mn}) and (f) intensity ratio of Mn to G band (I_{Mn}/I_G).

The band D' indicates the disorder and it is associated with finite-size graphite crystals and graphene edges. In brief, the strong D and D′ bands suggest presence of nanocrystalline structure,

graphene edges and defects including distortion, vacancies and micro-strain to graphitic lattices, which are all prevalent in disorder graphene [58, 59, 60, 61]. It is worthy to mention that the presence of defects and active edges in the graphitic lattices are kind of prerequisites for supporting the nucleation and growth of the assembled electroactive or redox nanoparticles and subsequently their electrochemical performance. On the other hand, rGO spectra indicates removal of C=O (carboxylic), C–O (epoxy) and C–O (alkoxy) groups, partial elimination of hydroxyl groups along with simultaneous restoration of carbon-carbon bonding. The remnants of hydroxyl groups are reported to be related to water molecules intercalated in-between graphene layers, which do not affect the hydrophobicity of graphene and usually improve electrical conductivity. Commonly, the integrated intensity ratio of D to G band (I_D/I_G) serve as a convenient measurement of the amount of defects and the size of the sp^2 C cluster or nanodomains that tends to increase during reduction of GO. Following Strohmeier and Hercules [62] and Kapteijn *et al*. [63] MnO_2 is Raman active, whereas Gosztola and Weaver [64] and Bernard *et al.*[65] reported well-defined spectra of this transition metal oxide. In our Raman spectra, MnO_2 has main features recognized at ~ 585 cm^{-1} and ~ 640 cm^{-1}. The band at ~ 580 cm^{-1} observed is attributed to Mn-O lattice vibrations in MnO_2, which is in good agreement with the bulk tetragonal MnO_2 phase [66, 43]. All of these spectra reflect the formation of MnO_2/GO and MnO_2/rGO hybrid films. For symmetry considerations, the band at ~ 650 cm^{-1} is assigned as E_{1g} mode and it is attributed to the stretching mode of Mn–O bond in MnO_6 octahedra shared by corners and/or edges in its crystal structure [67, 68]. Moreover, Raman scattering in MnO_2 arises from a collective vibration mode of the MnO_6 octahedron. The peaks at lower wavenumber correspond to the deformation modes of the metal–oxygen chain of Mn–O–Mn in the MnO_2 octahedral lattice sites. Since the manganese atom is about five times heavier than the oxygen atoms, the vibrations of the Mn–O groups are supposed to involve mainly the oxygen atoms.

Raman spectra are analyzed in terms of G (ω_D), 2D (ω_{2D}), Mn (ω_{Mn}) band position, the intensity ratio of D to G (I_D/I_G), G to 2D (I_G/I_{2D}) and Mn to G (I_{Mn}/I_G) presented in Figs. 4b-4f. While for GO-based hybrids, the G band ranged between 1595–1602 cm^{-1}, the change in rGO-based material is minimal at 1593–1595 cm^{-1}, which is within the spectral resolution (Fig. 4b). On the other hand, the 2D band changes rather strongly with manganese oxides on GO (2620–2625 cm^{-1}) and rGO (2690–2610 cm^{-1}) supports (Fig. 4d). The intensity ratio of G and 2D bands (I_G/I_{2D}) show strong dependence with MnO_2 on GO (3–8) and rGO (2–8) supports (Fig. 4c). The variation of Mn peaks is marginally higher for rGO hybrid (589 cm^{-1} and 660 cm^{-1}) as compared with GO hybrid (585 cm^{-1} and 635 cm^{-1}) as compared with MnO_x (584 cm^{-1} and 633 cm^{-1}) by themselves (Fig. 4e). For I_{Mn}/I_G ratio, it is 0.35 for MnO_2/GO and 0.06 for MnO_2/rGO hybrids for both the MnO_2 related bands (Fig. 4f).

Analogous to spectroscopic studies, electrical measurements could provide complementary information on metal oxide−graphitic interfaces besides resistivity of *dc* electrical conductivity (σ_{dc}) of hybrids. Figure 5 provides the room temperature I-V measurements determining two-terminal resistance R_{2t} and the corresponding σ_{dc} for hybrids and MnO_2 by itself. A few interesting noteworthy features from Fig. 5 are that the I-V curves showed quasi-semiconducting behavior in contrast to ohmic or linear behavior for MnO_2 and σ_{dc} of rGO and GO hybrids was comparable (0.6 S-cm) and much higher than those of MnO_2 (0.005 S-cm) as anticipated.

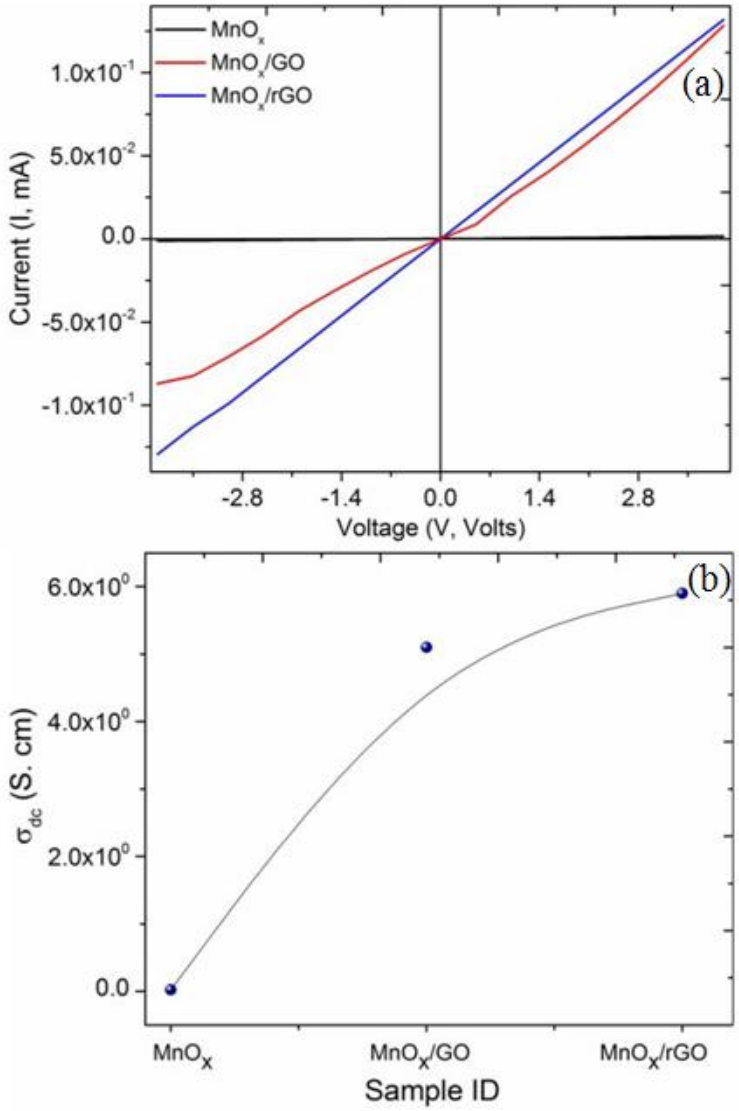

Figure 5. (a) Current *versus* voltage (I-V) plots for electrochemically synthesized MnO_x, MnO_x/GO and MnO_x/GO hybrids and (b) corresponding variation in room temperature dc electrical conductivity (σ_{dc}).

3.2 Electrochemical Supercapacitive Behavior

Figure 6 shows the CV curves for MnO_x (a) GO (b), rGO (c), MnO_x/GO (d) and (e) MnO_x/rGO measured in 1M Na_2SO_4 electrolyte at various scan rates. It is found that the capacitive contribution of bare C fiber cloth is negligible as compared with those of hybrid electrodes and the constituents. The CV curves for all of the hybrid electrodes show nearly rectangular shape and characteristic mirror-image with occasional redox peaks indicative of good ion response even at an exceeding high scan rate. Meanwhile, the MnO_x/GO and MnO_x/rGO electrodes show the larger integrated area of the CV curve than those of constituents' electrode and hence, it has the highest specific Cs. The Fig. 6f shows the variation of maximum current with square root of scan rate ($v^{1/2}$) of representative samples.

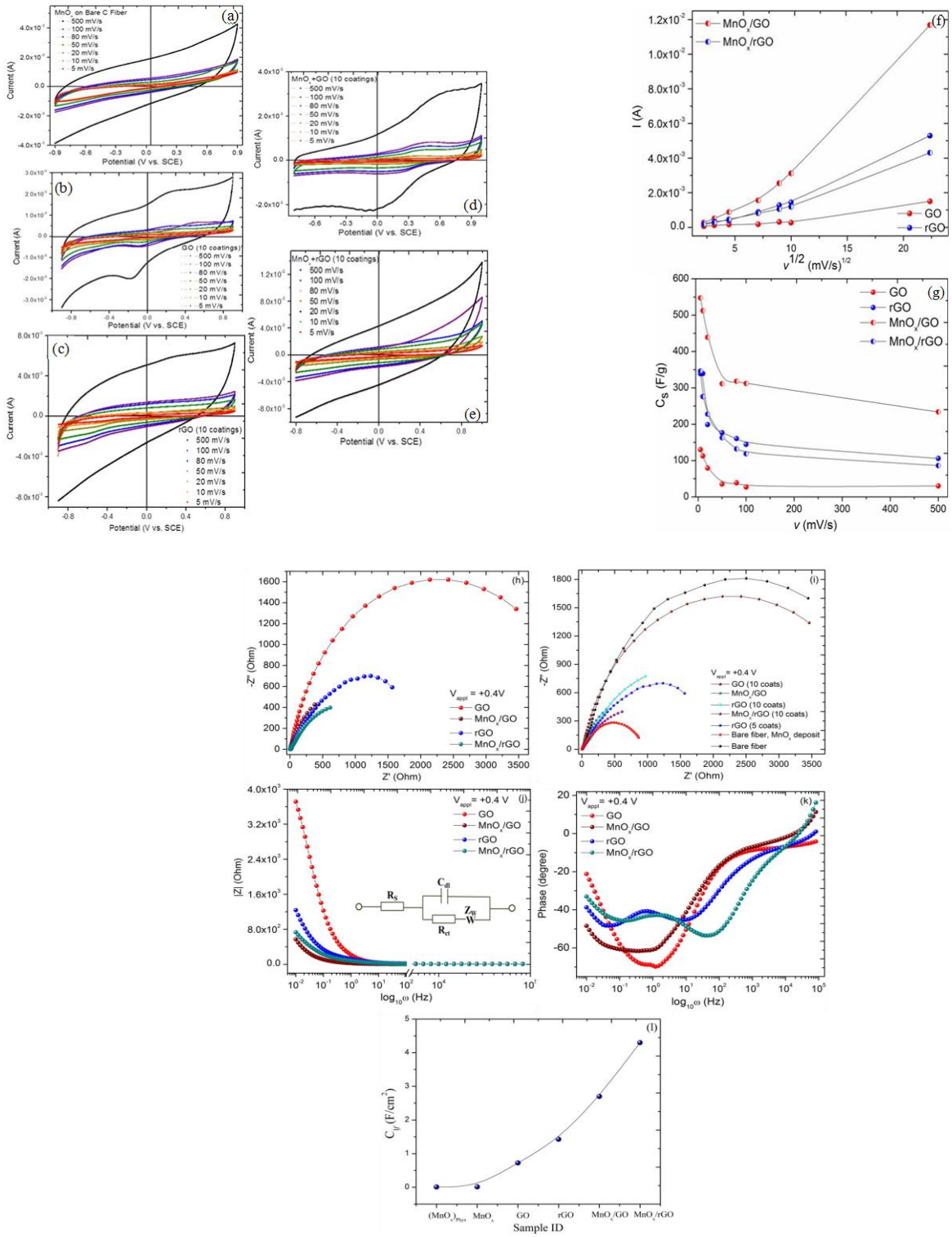

Figure 6. The cyclic voltammograms in 1M Na_2SO_4 electrolyte obtained from (a-e) MnO_x, GO, rGO, MnO_x/GO and MnO_x/rGO hybrids at scan rates of 5, 10, 20, 50, 80, 100 and 500 mV/s between potential window from –0.8 to +1.0 V (f) Variation of peak current with (scan rate)$^{1/2}$ and (g) specific capacitance C_s (F.g^{-1}) with scan rate. (h, i) Nyquist plots (j) Bode-Bode plots (Z magnitude) and (k) phase change, with $\log_{10}$ ω, for representative samples of GO, rGO, MnO_x, MnO_x/GO and MnO_x/rGO at V = +0.4 V revealing capacitive behavior. The equivalent RC circuit is also provided in inset (j). (l) Low-frequency area specific capacitance (C_{lf}) determined from impedance plots.

The magnitude of the current observed is governed by the Randles- Ševćik equation for a reversible transfer process: $I_{rev} = 0.446FAC\ (FDv\ /\ RT)^{0.5}$ or alternatively, for the case of fully irreversible electron transfer process: $I_{irrev} = 0.496\ (\alpha n')^{0.5}nFAC\ (FDv\ /\ RT\ )^{0.5}$, where A is the geometric area of the electrode (cm^2), α is the transfer coefficient (usually presumed to be 0.5), *F* is Faraday Constant (C mol^{-1}), *D* is diffusion coefficient (cm^2/s), *C* is concentration (mol/cm^3), *v* is scan rate (V/s), R and T are usual constants, n is the total number of electrons transferred in the electrochemical process and n' is the number of electrons transferred before the rate determining step. While GO shows almost linear behavior indicative of diffusion-limited phenomena, the curves for rGO, MnO_x/GO and MnO_x/rGO started to show non-linear behavior reflective of heterogeneous diffusion behavior. Figure 6g presents the variation in the specific capacitance with scan rate for GO, rGO, MnO_x/GO and MnO_x/rGO electrodes. As observed, all electrodes show gradual decrease in C_s with increasing scan rate. The highest Cs values for MnO_x/GO, MnO_x/GO, rGO, GO and MnO_x electrodes at a scan rate of 10 mV s^{-1}, are 560, 350, 150 and 70 Fg^{-1}, respectively. Hence, the presence of underlying GO and rGO films provides more electrochemical (re)active sites for the redox reaction of manganese dioxide.

To understand the reasons behind the unique capacitive performance of hybrid electrodes compared to constituent MnO_2 electrode, a comparative electrochemical impedance spectroscopy (EIS) data were also collected to quantify the electronic and ionic conductivity behavior and diffusive behavior of the MnO_2-based films besides determining the electric-double layer capacitance (C_{dl}), charge transfer resistance (R_{ct}) and low frequency (C_{lf}) capacitance. Nyquist plots of as-prepared hybrid MnO_x/GO and MnO_x/rGO and GO, rGO and MnO_x electrodes were measured in 1M Na_2SO_4 electrolyte over the frequency range from 10 mHz to 100 kHz as shown in Fig. 6h-6i. The Nyquist plots of these electrodes are closer to an ideal supercapacitor, which have a straight line in the low-frequency region and a small arc in the high-frequency region. In principle, the highest frequency intercept at the real component of impedance (Z') at the beginning of the arc represents the equivalent series resistance (ESR) [69], which consists of various contributions including the ionic resistance of the electrolyte (R_s), intrinsic resistance of the active material, intrinsic resistance of current collector and contact resistance at the interface between active material and current collector. The power density of supercapacitors depends strongly on the ESR [70]. The arc in the high-frequency region corresponds to the R_{ct} caused by the charge transfer process (*e.g.* Faradaic reactions) and electric double layer charging on the electrode surface and its magnitude is derived from arc diameter [71]. The line at low-frequency region is a result of ion diffusion transport from the electrolyte to the electrode surface [52]. The trend in increasing slope exhibits the capacitive nature related to the film charging mechanism, typical characteristic for porous framework electrodes.

The impedance data presented in Fig. 6 were analyzed using CHI software integrated with the electrochemical workstation. The equivalent RC circuit model proposed for analyzing the impedance data is in Fig. 6j inset. The model consists of R_s combined with interface resistance which represents ESR value, R_{ct}, C_{dl}, W, Warburg impedance and C_s, pseudo-capacitance. The fitting results show that the ESR values for MnO_2, GO, rGO, and MnO_2/GO and MnO_2/rGO electrodes are 2.04, 2.11, 1.92, 2.61 and 2.42 Ω, respectively. This refers that the contact resistance affects ESR with the presence of underlying GO and rGO support compared with MnO_2 film. The corresponding R_{ct} values are 3.28,

2.81, 3.01, 0.83 and 0.52 Ω, respectively, reflecting the enhancement in the electronic and ionic conductivities of MnO_2 with the presence of GO and rGO nanosheets. Finally, the slope of the Nyquist plots in the low-frequency region tends to increase with the presence of underlying GO and rGO films as compared with its absence, reflecting a decrease in the Warburg resistance (W) or fast electrolyte ion diffusion into the hybrid composites. The Fig. 6l shows area low frequency capacitance variation derived following $C_{lf} = 1/2\pi fZ$". Finally, the energy density ($E = 1/2\ CsV^2$/m) and power density ($P = V^2/4mR_S$) values of MnO_2/GO and MnO_2/GO electrodes estimated from C_s at charging–discharging current density of 1 mA cm^{-2} are 115 W kg^{-1} (105 W kg^{-1}) and 1104 Wh kg^{-1} (1017 Wh kg^{-1}), respectively. In brief, the improvement in the capacitive performance of MnO_2 film is determined with the presence of underlying GO and rGO sheets creating more active sites and tailored interfaces with MnO_2, facilitating the access of electrolyte ions and makes electron transport between GO (and rGO) and MnO_2 easier as confirmed by the results obtained from EIS data.

3.3 Scanning Electrochemical Microscopy

Electrochemistry is an interfacial technique dominated by surface and interfacial dynamics and reactivity processes occurring at solid/liquid interface. Optimizing energy storage and detailed mechanistic understanding at electrode/electrolyte interface are critical for their advancement. Recent studies showed that the graphene surface favor charge transfer surface adsorption sites including structural defects, imperfections and heterogeneity disrupting sp^2 C conjugation speculating that the larger defects sites concentration, interfaces and/or edge sites are relatively more reactive than those of pristine or clean surfaces [72]. Therefore, it is conceivable to investigate the nature of physical-chemical processes over hybrid electrodes surface. While CV characterizes the effective electrode areas comparable to geometric areas, SECM allows electrochemical currents to be mapped across electrode surface correlating with the structure in-situ and probe charge (ionic and electronic current; IC and EC) transport in contrast to other scanning probe microscopy techniques [73 ,74]. Among several operation modes, the visualization of the electrochemical activity is performed in feedback mode taking advantage of positive feedback over conductive/electrochemically active areas *versus* negative feedback over insulating/non-conductive/ relatively electrochemically inactive areas of the surface [74]. By detecting redox reactions occurring in small region in close proximity to electrode surface, SECM is used to obtain chemical reactivity images, local quantitative information of reaction rates (Fig. 7) and determine adsorption sites areal density (Fig. 7).

Figure 7c provides probe approach curves for hybrids with normalized distance, L = d/a, where d is substrate (electrode)-tip distance and a, the radius of the tip. The tip electrode current (i_T) reaches asymptotic behavior with steady-state current following: $i_{T,\infty} = 4nFCDa$, where n is the number of electrons transferred at the electrode tip ($O + ne^- \rightarrow R$), F is Faraday's constant, C is concentration or flux of oxidized species and D is the diffusion coefficient limited by hemispherical region. With tip approaching conductive region of the heterogeneous electrode surface, the reduced species formed at the tip is oxidized at the conductive surface, yielding an increase in the tip current ($i_T > i_{T,\infty}$) and creating a regenerative "positive" feedback loop. The opposite effect is observed when probing

insulating region and diffusion to the electrode is inhibited as a result of physical obstruction as the tip approaches the substrate, creating a "negative" feedback loop thus decreasing the tip current ($i_T < i_{T,\infty}$) [74,75]. Thus the total tip current is given by: $i_T = nFDC\ \pi a^2/d + 4nFDCa$, where the symbols have usual meaning. The first term is reminiscent of extent of concavity (or convexity) of probe approach curves plotted in Fig. 7c as solid curves and the second term helped to determine D that ranged between 1 x 10^{-8}–3 x 10^{-6} m^2 s^{-1} in the order (MnO_x/GO) > (MnO_x/rGO).

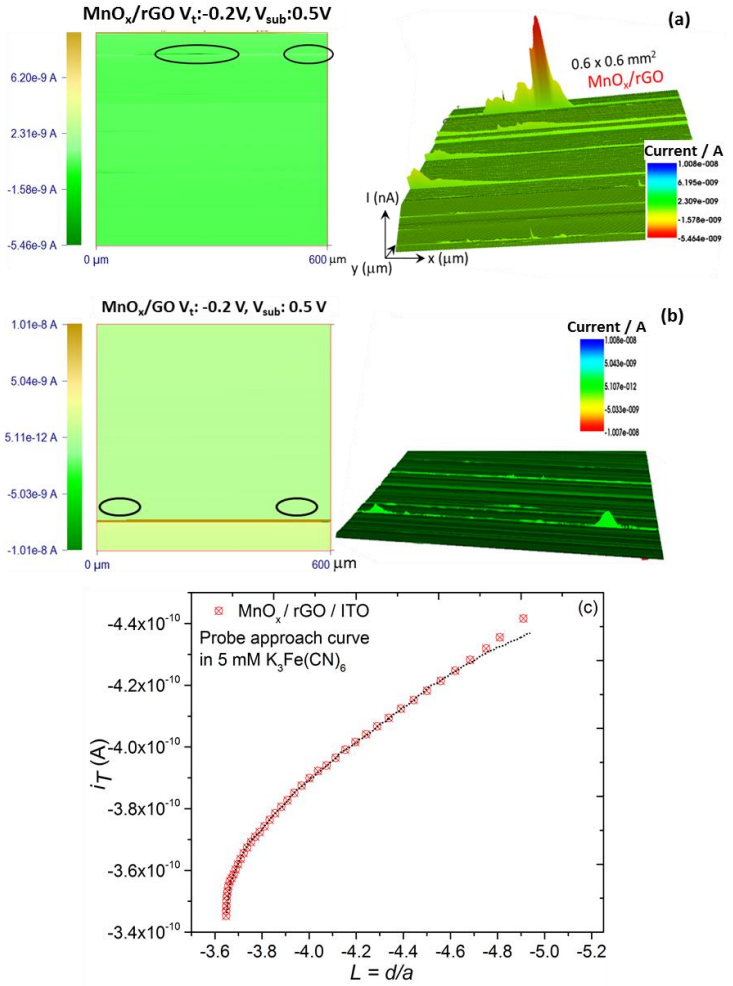

Figure 7. The scanning electrochemical microscopy (SECM) of representative (a) MnO_x/rGO and (b) MnO_x/GO hybrid samples displaying probe current distribution in 2D and 3D with occasional higher/lower current "highly reactive" electrochemical sites along with (c) probe approach curve for MnO_x/rGO indicative of semiconductive/insulating behavior at the solid/liquid interface in redox mediator 10 mM $K_3Fe(CN)_6$ (potassium ferricyanide; $Fe(CN)_6^{3-}$) in support electrolyte 1M KCl at tip voltage of V_t = –0.2 V and substrate voltage V_s = 0.5 V. A color bar is shown for quantitative values of the current.

Figure 7 also displays SECM area scans in two- and three-dimensions, where probe current is graphed as a map for (MnO_x/rGO) and (MnO_x/GO) films as representative example. The probe was polarized at potential sufficient to cause an electrochemical reaction (generator) and the current was recorded over the polarized electrode surface. The changes in the electrochemical activity (or heterogeneous electron transfer) give an electrochemical reaction (generator) and the current was

recorded over the polarized electrode surface (collection). The higher and lower surface current is characteristic of metal/insulating/semiconducting behavior at the solid/liquid (or electrode/electrolyte) interface. It is apparent from the probe current distribution that both the samples yielded occasional relatively higher values of probe current reinforcing the role played by both GO and rGO platelets along with MnO_x nanoparticles in providing more (re)active sites.

4. CONCLUSION

We have demonstrated the successful preparation of graphene/manganese dioxide hybrid electrodes *via* potentiodynamic cycling deposition of semi-crystalline MnO_x film on pre-deposited graphene derivatives coated on carbon fiber cloth and ITO as substrates from aqueous solution of GO and rGO colloidal dispersions. Raman spectroscopy and other complementary structural analytical techniques confirmed that the electrochemical process enables the formation of MnO_2 on overlapped and stacked platelets of GO and rGO nanosheets having sufficient electrochemically active sites. The hybrids and constituent electrodes performance was characterized as asymmetric supercapacitors. It was found that the presence of underlying GO and rGO films loaded with optimized MnO_2 nano-aggregates increased the specific capacitance of the films with Cs of 560 Fg^{-1} (and 350 Fg^{-1}) and R_{ct} of 0.52 Ω (and 0.83 Ω) for MnO_2/GO (and MnO_2/rGO) electrodes. These MnO_2/GO and MnO_2/rGO hybrid electrodes exhibited power density of 1017 W kg^{-1} and 1104 W kg^{-1} and corresponding energy density of 115 Wh kg^{-1} and 105 Wh kg^{-1}, respectively. The large specific surface area and marginally defective nature of graphene derivatives in conjunction with an efficient utilization of MnO_2 nanoparticles facilitated rapid ion transport and electrochemical cyclic stability. In addition, the SECM allowed to visualize hybrid surfaces electrochemically reactive adsorption sites and to investigate electrode/electrolyte interfaces determining diffusion constant.

ACKNOWLEDGEMENTS

The author (S.G.) gratefully acknowledges financial support in parts from WKU Research Foundation for start-up funds and NSF EPSCoR Track RII Award (EPS-0814194 and 3048108525-l4046). The authors (S.G. and M.vM.) also acknowledge the WKU Research Foundation for awarding an internal Research grant. We thank Carson Price and Dr. J. Andersland for help in some of the TEM measurements.

References

1. R. Kötz, M. Carlen, *Electrochimica Acta*, 45 (2000) 2483.
2. L.-Q. Mai, F. Yang, Y.-L. Zhao, X. Xu, L. Xu, Y.-Z. Luo, *Nature Communication*, 2 (2011) 381.
3. A.K. Geim, K.S. Novoselov, *Nature Materials*, 6 (2007) 183.
4. S. Gupta, E. Heintzman, J. Jasinski, *Journal of Electronics Materials*, 43 (2014) 3458 and references therein.
5. Y. Zhang, Y.-W. Tan, H. L. Stormer, P. Kim, *Nature*, 438 (2005) 201.
6. C. Lee, X. D. Wei, J. W. Kysar, J. Hone, *Science*, 321 (2008) 385.
7. M. D. Stoller, S. Park, Y. Zhu, J. An, R. S. Ruoff, *Nano Letters*, 8 (2008) 3498.
8. C. Liu, Z. Yu, D. Neff, A. Zhamu, B. Z. Jang, *Nano Lett.* 10 (2010) 4863.
9. Hou, Y. Shao, M. Ellis, B. R. Moore, B. Yi, *PCCP* 13 (2011) 15384.
10. K. P. Loh, Q. L. Bao, P. K. Ang, J. X. Yang, *Journal of Materials Chemistry*, 20 (2010) 2277.
11. K. P. Loh, Q. Bao, G. Eda, M. Chowalla, *Nature Chemistry* 2 (2014) 1015 and references therein.
12. G. Eda, M. Chowalla, *Advanced Materials* 22 (2010) 2392 and references therein.
13. A. J. Du, Z. H. Zhu, S. C. Smith, *Journal of the American Chemical Society*, 132 (2010) 2876.
14. Q. Zhang, E. Uchaker, S. L. Candelaria, C. Guozhong, *Chemical Society Review*, 42 (2013) 3127 (2013).
15. B. E. Conway, *Electrochemical Supercapacitors: Scientific Fundamentals and Technological Applications*, Kluwer Academic, Plenum Publishers, New York (1999).
16. L. Nyholm, G. Nyström, A. Mihranya, M. Strømme, *Advanced Materials*, 23 (2011) 3751.
17. J. T.-Wei Wang, J. M. Ball, E. M. Barea, A. Abate, J. A. A.-Webber, J. Huang, M. Saliba, I. M.-Sero, J. Bisquert, H. J. Snaith, R. J. Nicholas, *Nano Letters*, 14 (2014) 724.
18. M. Liu, R. Zhang, W. Chen, *Chemical Review*, 114 (2014) 5117.
19. B. Luo, S. M. Liu, L. J. Zhi, *Small*, 8 (2012) 630.
20. S. Gupta, A. Irihamye, *AIP Advances*, 5 (2015) 037106 and references therein.
21. P. Blake, P. D. Brimicombe, R. R. Nair, T. J. Booth, D. Jiang, F. Schedin, L. A. Ponomarenko, S. V. Morozov, H. F. Gleeson, E. W. Hill, A. K. Geim, K. S. Novoselov, *Nano Letters*, 8 (2008) 1704.
22. I. V. Pavlidis, T. Vorhaben, D. Gournis, G. K. Papadopoulos, U. T. Bornscheuer, H. Stamatis, *Journal of Nanoparticle Research*, 14 (2012) 842.
23. D. A. Dikin, S. Stankovich, E. J. Zimney, R. D. Piner, G. H. B. Dommett, G. Evmenenko, S. T. Nguyen, and R. S. Ruoff, *Nature*, 448 (2007) 457.
24. J. T. Robinson, M. Zalalutdinov, J. W. Baldwin, F. K. Perkins, E. S. Snow, Z. Wei, P. E. Sheeshan, B. H. Houston, *Nano Letters*, 8 (2008) 3441.
25. J. T. Robinson, F. K. Perkins, E. S. Snow, Z. Wei, P. E. Sheeshan, *Nano Letters*, 8 (2008) 3137.
26. X. Zuo, S. He, D. Li, C. Peng, Q. Huang, S. Song, C. Fan, *Langmuir*, 26 (2010) 1936.
27. C. Jafta, F. Nkosi, L. Roux, M. Mathe, M. Kebede, K. Makgopa, Y. Song, D. Tong, M. Oyama, N. Manyala, S. Chen, K. Ozoemena, *Electrochimica Acta*, 110 (2013) 228.
28. A. H. C. Neto, F. Guinea, N. M. R. Peres, K. S. Novoselov, and A. K. Geim, *Reviews of Modern Physics*, 81 (2009) 109.
29. J. Xia, Q. Kuang, S. Yang, F. Xia, S. Wang, L. Guo, *Scientific Reports* 3 (2013) 2300 and references therein.
30. L. Wang, Y. Li, Z. Han, L. Chen, B. Qian, X. Jiang, J. Pinto, G. Yang, *Journal of Materials Chemistry A*, 1 (2013) 8385.
31. J. A. Roger, Y. G. Huang, *Proceedings of the National Academy of Sciences USA*, 106 (2009) 10875.
32. D. H. Kim, N. Lu, R. Ma, Y. S. Kim, R.H. Kim, S. Wang, J. Wu, S. M. Won, H. Tao, A. Islam *et al. Science*, 333 (2011) 838.
33. V. V. N. Obreja, *Physica E*, 40E (2008) 2596.

34. E. Frackowiak, F. Béguin, *Carbon*, 39 (2001) 937.
35. C. Peng, S. Zhang, D. Jewell, G. Z. Chen, *Proceedings of National Sciences*, 18 (2008) 177.
36. W. Sugimoto, K. Yokoshima, Y. Murakami, Y. Takasu, *Electrochimica Acta*, 52 (2006) 1742.
37. P. Simon, Y. Gogotsi, *Nature Materials*, 7 (2008) 845.
38. M. Mecklenburg, A. Schuchardt, Y. K. Mishra, S. Kaps, R. Adelung, A. Lotnyk, L. Kienle, K. Schulte, *Advanced Materials*, 24 (2012) 3486.
39. Y. Sun, X. Hu, W. Luo, Y. Huang, *ACS Nano*, 5 (2011) 7100.
40. Y. Liang, Y. Li, H. Wang, H. Dai, *Journal of the American Chemical Society*, 135 (2013) 2013.
41. J. Zhang, J. Jiang, X. S. Zhao, *Journal of Physical Chemistry C*, 115 (2011) 6448.
42. G. Aminoff, *Zeitschrift für Kristallographie,* 64 (1927) 475.
43. J. Attenburrow, A.F.B. Cameron, J.H. Chapman, R.M. Evans, B.A. Hems, A.B.A. Jansen, T. Walker, *Journal of Chemical Society*, 1094 (1952).
44. T. Nakajima, A. Mabuchi, R. Hagiwara, *Carbon*, 26 (1988) 357.
45. W. Scholz, H. P. Z. Boehm, *Zeitschrift für anorganische und allgemeine Chemie*, 369 (1969) 327.
46. J. Coraux, L. Marty, N. Bendiab, V. Bouchiat, *Accounts of Chemical Research*, 46 (2013) 2193.
47. Z. Xu, Z. Li, C. M. B. Holt, X. Tan, H. Wang, B. S. Amirkhiz, T. Stephenson, D. Mitlin, *Journal of Physical Chemical Letters*, 3 (2012) 2928.
48. S Gupta, M. van Meveren, J. Jasinski, *Journal of Electronics Materials*, 44 (2015) 62 and references therein.
49. F. Xiao, Y. Xu, *International Journal of Electrochemical Science*, 7 (2012) 7440.
50. S.-M. Chen, R. Ramachandran, V. Mani, R. Saraswathi, *International Journal of Electrochemical Science*, 9 (2014) 4072.
51. W Hummers, R. J. Offeman, *American Chemical Society*, 80 (1958) 1339.
52. S. Park, J. An, R. J. Potts, A. Velamakanni, S. Murali, R. S. Ruoff, *Carbon*, 49 (2011) 3019.
53. D. C. Marcano, D. V. Kosynkin, J. M. Berlin, A. Sintskii, Z. Sun, A. Slesarev, L. B. Alemany, W. Lu, J. M. Tour, *ACS Nano*, 4 (2010) 4806.
54. S. Greenwald, *Acta Crystallographica*, 6 (1953) 396.
55. W. L. Smith and A.D. Hobson, *Acta Crystallographica*, B29 (1953) 362.
56. K. Kobayashi, M. Tanimura, H. Nakai, A. Yoshimura, H. Yoshimura, K. Kojima, M. Tachibana, *Journal of Applied Physics*, 101 (2007) 94306.
57. M.S. Dresselhaus, G. Dresselhaus, R. Saito, A. Jorio, *Physics Reports*, 409 (2005) 47.
58. Y. Wu, P. Qiao, T. Chong, Z. Shen, *Advanced Materials*, 14 (2002) 64; Y. Wu, B. Yang, B. Zong, H. Sun, Z. Shen, Y. Feng, *Journal of Materials Chemistry*, 14 (2004) 469.
59. K. Shiji, M. Hiramatsu, A. Enomoto, M. Nakamura, H. Amano, M. Hori, *Diamond and Related Materials*, 14 (2005) 831.
60. S. Mori, T. Ueno, M. Suzuki, *Diamond and Related Materials*, 20 (2011) 1129.
61. L. G. Cançado, K. Takai, T. Enoki, M. Endo, Y.A. Kim, H. Mizusaki, A. Jorio, L.N. Coelho, R. Magalhaes-Paniago, M.A. Pimenta, *Applied Physics Letters*, 88 (2006) 163106.
62. B. R. Strohmeier, D. M. Hercules, *Journal of Physical Chemistry*, 88 (1988) 4923.
63. F. Kapteijn, A. D. Van Langeveld, J. A. Moulijn, A. Andreini, M. A. Vuurman, A. M. Turek, J-M. Jehng, I. E. Wachs, *Journal of Catalysis*, 150 (1994) 94.
64. D. Gosztola, M. J. Weaver, *Journal of Electroanalytical Chemistry Interfacial Electrochemistry*, 271 (1989) 141.
65. M. -C. Bernard, A. H.-Le Go, V. B. Thi, S. C.de Torresi, *Journal of Electrochemical Society*, 140 (1993) 3065.
66. C. Julien, M. Massot, R. Baddour-Hadjean, S. Franger, S. Bach, J. P. Pereira-Ramos, *Solid State Ionics*,159 (2003) 345.
67. I. Rusakova, T. O. Ely, C. Hofmann, D. P.-Centurion, C. S. Levin, N. J. Halas, A. Luttge, K. H. Whitmire, *Chemistry of Materials*, 19 (2007) 1369 (2649u).
68. C. M. Julien, M. Massot, *Journal of Physics of Condensed Matter*, 15 (2003) 3151.

69. Q. Lu, Y. Zhou, *Journal of Power Sources*, 196 (2011) 4088.
70. A. Celzard, F. Collas, J.F. Marêché, G. Furdin, I. Rey, *Journal of Power Sources*, 108 (2002) 153.
71. T. Tüken, B. Yazıcı, M. Erbil, *Progress in Organic Coatings*, 50 (2004) 115.
72. C. Tan, J. R. López, J.J. Parks, N.L. Ritzert, D. C. Ralph, H.D. Abruňa, *ACS Nano*, 6 (2012) 3070.
73. Y. Wang, K. Kececi, J. Velmurugan, M. V. Mirkin, *Chemical Sciences*, 4 (2013) 3606 and references therein.
74. R.L. Mcreery, *Chemical Reviews*, 108 (2008) 2646.
75. F. Montilla, M. A. Cotarelo, E. Morallon, *Journal of Materials Chemistry*, 19 (2009) 305.